Research Square

Preprints are preliminary reports that have not undergone peer review.
They should not be considered conclusive, used to inform clinical practice,
or referenced by the media as validated information.

Multisource constraints on lunar crater-to-basin transitions and implications for the evolution of the lunar hemispheric dichotomy

Quanxi Ge
Jilin University https://orcid.org/0009-0001-4930-3817
Changbao Yang
Jilin University
Liguo Han
hanliguo@jlu.edu.cn
Jilin University
Lezhen Han
Jilin University
Shiqin Yang
Jilin University
Yu He
Jilin University
Jiawen Chen
Jilin University

Research Article

Keywords: lunar impact craters, multi-source data, lunar hemispheric dichotomy, KREEP, peak-ring basins

Posted Date: August 7th, 2026

DOI: https://doi.org/10.21203/rs.3.rs-10612061/v1

License: This work is licensed under a Creative Commons Attribution 4.0 International License.
Read Full License

Additional Declarations: The authors declare no competing interests.

Multisource constraints on lunar crater-to-basin transitions and implications for the evolution of the lunar hemispheric dichotomy

Quanxi Ge[a], Changbao Yang[a], Liguo Han[a,*], Lezhen Han[a], Shiqin Yang[a], Yu He[a], Jiawen Chen[a]

[a] *College of Geo-Exploration Science and Technology, Jilin University, No. 938 Ximinzhu Street, Chaoyang District, Changchun, 130026, Jilin Province, P.R. China*

Abstract

The crater-to-basin transition records how impact energy couples to the lunar crust and upper mantle, but morphology-based basin classes do not necessarily coincide with the onset of a coherent geophysical response. Here we combined 13 co-registered lunar data layers on a 32 ppd global grid and analyzed six representative physical variables for 83 061 craters. Diameter binning, changepoint detection, and Monte Carlo uncertainty propagation identify a multisource geophysical transition scale centered at $D = 195 \pm 5$ km; farside and nearside estimates are 195 ± 5 km and 190 ± 5 km, respectively. The result is population-level rather than a redefinition of the traditional morphological classification boundary. Stacked normalized radial profiles of 6973 impact structures show gradual variations for smaller craters but stronger hemispheric contrasts among large basins. Nearside basins exhibit positive Bouguer gravity anomalies, subdued topography, FeO–TiO_2-rich in-

*Corresponding author. Tel.: +86 135 0470 3788
Email address: hanliguo@jlu.edu.cn (Liguo Han)

filling, and local day-night brightness-temperature contrasts, whereas farside basins retain stronger highland signatures. Normalized by main-ring radius R, farside and nearside peak-ring radii are $0.46R$ and $0.49R$; characteristic geophysical proxy zones occur near $0.61R$ and $0.89R$–$0.95R$. These patterns indicate that large impacts sampled and modified pre-existing hemispheric differences in lunar thermal structure and composition.

Keywords: lunar impact craters, multi-source data, lunar hemispheric dichotomy, KREEP, peak-ring basins

---

1. Introduction

The lunar surface preserves one of the most continuous records of impact cratering in the Solar System. Impact craters and peak-ring basins across a wide range of sizes record the impact flux and surface-modification history, while retaining information on early crustal thickness, thermal state, target composition, and later volcanism. Classical impact theory relates transient-cavity excavation, impact-melt volume, and final crater morphology to impact energy, target-crust strength, and gravity. In particular, the scaling between transient-cavity radius and final crater diameter provides a basis for identifying post-impact collapse, peak-ring formation, and modification of basin margins (Melosh and McKinnon, 1978; Melosh, 1980, 1989; Cintala and Grieve, 1998). Numerical models generally define the transient crater at the time when the excavated cavity reaches its maximum volume. Potter et al. further showed that the position of the crustal annular bulge beneath a basin can provide an independent constraint on transient-crater radius, although this relationship varies with the thermal state of the pre-

impact crust and upper mantle (Potter et al., 2012). Because the Moon has experienced neither substantial atmospheric erosion nor plate-tectonic recycling, post-impact topographic collapse, peak rings, Moho uplift, and ejecta emplacement can remain preserved over geological timescales. Lunar impact basins therefore provide natural cross-sections through the early lithospheric evolution of terrestrial bodies.

Early studies of lunar impact structures relied primarily on image interpretation and topographic measurements, leading to classification schemes based on diameter, depth, crater-wall collapse, central peaks, and ring structures. By diameter, impact structures can be divided into simple bowl-shaped craters ($D < 10$ km), transitional craters ($10 \leq D < 30$ km), complex craters ($30 \leq D < 200$ km), peak-ring basins ($200 \leq D < 550$ km), and multi-ring basins ($D \geq 550$ km); mare and highland craters can also be distinguished by geological setting (Wood and Anderson, 1978; Heiken et al., 1991; Stöffler et al., 2006; Neumann et al., 2015; Yue et al., 2023). This framework captures the principal morphological sequence from crater-wall collapse and central-peak development to peak-ring formation and multi-ring faulting. The diameter boundaries, however, remain sensitive to the preservation state and classification criteria. Jiang et al. described the development of lunar crater identification from manual interpretation to integrated approaches that combine imagery, digital elevation models, and automated algorithms, while emphasizing that catalog quality control, scale dependence, and geological interpretation still require reliable morphological constraints (Jiang et al., 2024). LOLA topography enables depth-to-diameter ratios, annular slopes, and basin-rim relief to be compared on a common datum, but to-

pography alone cannot readily distinguish primary excavation from basaltic infilling, viscoelastic relaxation, or overprinting by secondary impacts.

Morphological classifications are intuitive and suitable for global cataloging, but their diameter ranges record the final preserved form of an impact structure rather than the depth of energy coupling during impact. Mare basalts may bury or smooth the original rims and peak rings of nearside basins, whereas secondary impacts and ejecta overprinting can weaken local boundaries in old farside basins. A transition diameter based only on morphology, or an empirical peak-ring-to-rim ratio applied without additional constraints, may therefore conflate the primary impact response with post-impact modification (Pike, 1980; Baker et al., 2011).

Gravity observations provide an independent constraint on the deep structure of impact basins. The GRAIL mission substantially improved lunar gravity-field models and revealed relationships among mascon basins, crustal-thickness variations, Moho relief, and deep mass anomalies (Wieczorek et al., 2013; Zuber et al., 2016). Neumann et al. further used Bouguer anomalies to identify lunar impact basins, reducing reliance on visual morphological classification for interpreting basin boundaries and subsurface structure (Neumann et al., 2015). Basin gravity anomalies can be influenced not only by excavation depth but also by pre-impact porosity, lithospheric thermal structure, and later loading (Milbury et al., 2015; Dombard et al., 2013; Freed et al., 2014). Joint morphology-gravity analyses thus provide strong constraints on basin mechanics, but most previous studies have focused on individual basins or small sets of representative structures.

The transition from impact craters to basins is not determined by geomet-

ric diameter alone. Smaller complex craters are dominated by crater-wall collapse, central-peak development, and localized melting. With increasing size, the transient-cavity radius, peak-ring radius, main basin margin, and Moho rebound collectively contribute to the final morphology (Melosh and McKinnon, 1978; Baker et al., 2011; Neumann et al., 2015). Potter's simulations indicate that inward and downward motion during transient-cavity collapse localizes strain and produces normal-fault-like structures in unmelted rock outside the cavity. When the cavity penetrates the lithosphere and reaches the asthenosphere, inward asthenospheric flow can drag the overlying lithosphere and promote outer ring faulting; the resulting fault geometry depends on the thermal structure of the target crust (Potter, 2015). Published onset diameters therefore vary with the morphological element, gravity signature, or regional population emphasized in each study. The same structure may be classified morphologically as a large complex crater while already exhibiting a basin-scale deep response in gravity data. A common data framework is needed to recalibrate the radial relationships among the transient cavity, peak ring, and main basin margin when assessing global lunar thermomechanical differentiation.

Previous crater-to-basin transition criteria have consequently been based mainly on morphology and gravity. Morphology describes preserved surface geometry, whereas gravity constrains subsurface mass distribution. Together they resolve structural changes with increasing basin size, but they do not independently determine whether a stable deep-response transition exists in the global population, whether mass anomalies change in concert with composition, magnetic anomalies, thermal state, and permittivity, or whether

a transition is controlled mainly by impact energy, target-crust thermal state, or later volcanic infilling. These ambiguities are particularly important in the context of the lunar hemispheric dichotomy, because the Procellarum KREEP Terrane, the feldspathic farside highlands, mare-basalt infilling, and preservation of a cold, thick crust can each alter the interpretation of an isolated morphological or gravity indicator.

Geochemical remote sensing provides complementary constraints on material composition. Lunar Prospector gamma-ray spectrometer data map the global distributions of Th, K, U, FeO, and TiO_2, enabling the compositions of the Procellarum KREEP Terrane, mare basalts, feldspathic highlands, and South Pole-Aitken basin to be distinguished (Prettyman et al., 2006; Lawrence et al., 2003; Korotev et al., 2003). The lunar crustal terranes defined by Jolliff et al. emphasize genetic relationships among the KREEP-rich nearside, feldspathic farside highlands, and large impact basins (Jolliff et al., 2000). Models of ejecta thickness and compositional mixing further indicate that large impacts transport deep or distal material beyond the crater rim, producing annular anomalies over measurable distances (McGetchin et al., 1973; Xiao et al., 2021). Compositional anomalies, however, may reflect pre-impact crustal differences, ejecta mixing, and later mare-basalt coverage. Without gravity and topographic constraints, elemental distributions alone provide non-unique estimates of excavation depth and crust-mantle exchange.

The nearside-farside dichotomy further amplifies this uncertainty. Enrichment of heat-producing elements in the Procellarum KREEP Terrane maintained higher temperatures in the nearside crust and upper mantle (Wieczorek and Phillips, 2000). Impact simulations show that otherwise equivalent

impacts can produce a larger region of crustal thinning in a warm, weak nearside crust than in a cold, mechanically strong farside crust (Miljković et al., 2013). Nearside basins may therefore undergo more extensive collapse, magmatic infilling, and viscoelastic relaxation, whereas the cold, thick farside crust is more favorable for preserving primary excavation boundaries and ring faults. Final topography or a single elemental abundance cannot readily separate pre-existing hemispheric crustal differences from the effects of impact and post-impact modification. Establishing a global transition scale requires gravity, morphology, composition, and thermal-dielectric properties to be evaluated together.

Magnetic, radar, and microwave observations provide additional constraints on surface and subsurface physical properties. Lunar magnetic anomalies measured by missions including SELENE can be used to assess remanent magnetization, impact-induced demagnetization, and localized magnetized structures (Tsunakawa et al., 2014). Radar observations have been used to estimate regolith thickness, rock abundance, and dielectric properties, linking circular polarization ratio and radar scattering to the physical state of the lunar regolith (Shkuratov and Bondarenko, 2001; Fa et al., 2011; Fa and Cai, 2013). Chang'E microwave radiometer observations constrain thermal inertia, density, and dielectric loss through brightness temperature, and existing models describe its variation with time, frequency, and regolith thickness (Fa and Jin, 2010, 2007; Feng et al., 2010). Recent sample measurements and simulations also show that FeO, TiO_2, porosity, and temperature affect the effective complex permittivity and dielectric loss tangent of the regolith (Fa and Wieczorek, 2012; Fa, 2023; Kobayashi et al.,

2023). These studies extend crater analysis into additional physical-property domains, but most applications still emphasize radar, microwave, or dielectric data individually rather than comparing them directly with topography, gravity, and composition.

Collectively, previous studies have established complementary views of lunar impact structures: morphological studies resolve crater geometry and ring structure; gravity studies constrain Moho rebound and mass anomalies; geochemical studies trace KREEP, FeO, TiO_2, and feldspathic materials; and magnetic and microwave observations provide information on remanence, thermal inertia, and dielectric properties. A common limitation is that most studies use a single data source or compare only two datasets. Morphology-gravity analyses constrain basin mechanics, composition-topography comparisons help distinguish ejecta from basaltic coverage, and microwave-dielectric models characterize subsurface thermophysical properties. These single-source or paired frameworks, however, cannot readily test whether morphology, deep mass distribution, composition, magnetic anomalies, and thermal-dielectric properties share a common scale-dependent transition.

The datasets also differ in spatial resolution, projection, and sampling grid. Direct cell-by-cell comparisons of native products can be affected by pixel scale, interpolation, and geographic co-registration errors. Crater diameters span tens to thousands of kilometers, and annular responses among physical variables cannot be compared directly without a common spatial grid and normalized radial coordinate. The Robbins global lunar crater database enables population-scale analyses (Robbins, 2019), but a reproducible framework is required to integrate this catalog with multiple physical-

property datasets and thereby assess impact-basin evolution.

The value of multi-source observations therefore lies not only in the number of datasets, but in evaluating distinct physical processes along a common scale axis. Topographic elevation records the preserved morphology and degree of post-impact infilling; the Bouguer gravity anomaly constrains subsurface mass distribution and Moho response; FeO and Th trace mafic basaltic material and KREEP-rich components, respectively; and real permittivity and midnight microwave brightness temperature jointly reflect regolith compaction, dielectric loss, and subsurface thermal inertia. A transition that appears coherently in these variables provides stronger evidence for a population-level geophysical change than a changepoint in any single curve. Conversely, deviations of an individual variable from the common trend may identify local effects of basaltic infilling, ejecta mixing, or hemispheric thermal structure.

Here we integrate 13 data layers on a common 32 ppd global lunar grid. Unlike previous single-source or two-source comparisons, all physical fields are co-registered in the same projection, spatial resolution, and crater-centered radial coordinate. The analysis retains the traditional morphological and gravity context while adding compositional, thermal, magnetic, and dielectric constraints on the transition scale. We first analyze the global diameter-binned crater population and then construct stacked normalized radial profiles for nearside and farside structures above and below the transition scale. The objectives are to identify a characteristic multi-source geophysical transition from shallow morphological response to deeper basin-scale response; distinguish this transition scale from a purely morpho-

logical classification boundary; recalibrate the relationships among peak-ring radius, main basin diameter, transient-cavity radius, and final basin radius; and assess how impact basins record the lunar hemispheric dichotomy and post-impact modification.

2. Results

2.1. Transition scale in the crater-diameter spectrum

Across the 83 061 global craters with diameters greater than 5 km, the six variables selected from the 13 data layers show coordinated changes near $D = 195$ km (Fig. 1); the bin definitions are listed in Supplementary Table 1. This value lies within B20 ($190 \leq D < 200$ km), is defined by the bin midpoint, and is the principal transition diameter identified by both segmented regression and Fisher optimal partitioning for the global sample. Monte Carlo results for the 240 km search limit are given in Table 1. The two PCA-weighted methods yield a joint support probability of 0.826 for the global characteristic transition scale of 195 ± 5 km, with a 95% confidence interval of 165–205 km. The transition is therefore identified from the covariance of six physical variables across the crater population, not from the value of an individual bin alone. Below this scale, topographic elevation decreases slightly with diameter, whereas the Bouguer gravity anomaly, FeO abundance, Th abundance, real part of permittivity, and midnight brightness temperature change more gradually. Near $D = 195$ km, these variables change from gradual trends to larger bin-to-bin variability.

The hemispheric results show different probabilistic support for the transition scales (Fig. 2 and Table 1). For the original farside bins, B20 is the

dominant bin and the support probability for 195 ± 5 km is 0.913, with a 95% confidence interval of 185–195 km. For the nearside bins shifted by 5 km, B19 is dominant and the support probability for 190 ± 5 km is 0.618, with a 95% confidence interval of 150–200 km. The narrower farside interval and higher support probability show that the farside population contributes more strongly to the global 195 km result.

Sensitivity to the upper search limit shows that the PCA-weighted global result remains in the 190–200 km bin when the limit is extended to 1000 km, although its support probability decreases from 0.826 to 0.237. At limits of 1500 and 2600 km, the dominant scales shift to 450 and 600 km, respectively, reflecting the entry of very large multi-ring basins into the search space. The farside analysis returns 195 km at every upper limit, with support probabilities decreasing from 0.913 to 0.438, whereas the dominant nearside scale shifts to larger diameter bins when the upper limit exceeds 300 km. Complete results are provided in Supplementary Table 3.

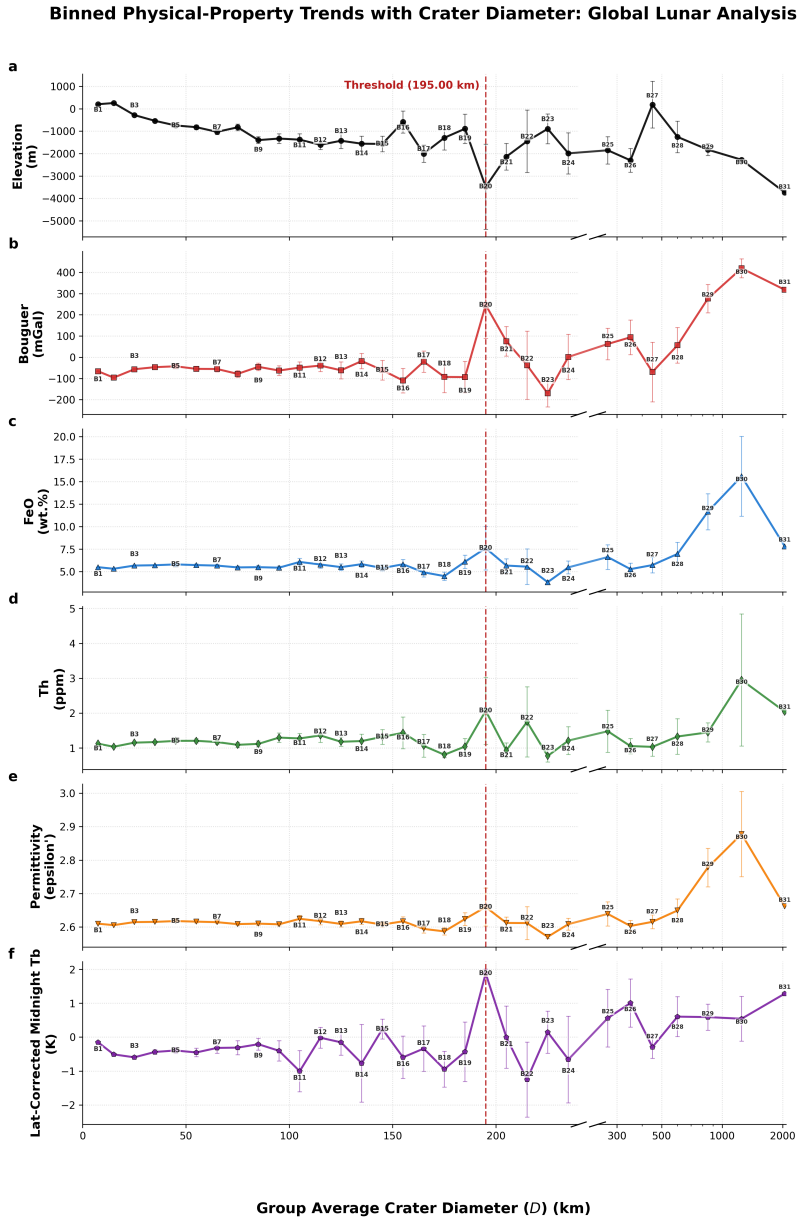


Figure 1: Diameter-binned means of six physical variables for the global crater population. (a) Topographic elevation; (b) Bouguer gravity anomaly; (c) FeO abundance; (d) Th abundance; (e) real part of the effective complex permittivity; and (f) latitude-corrected midnight microwave brightness temperature. The original bins listed in Supplementary Table 1 are used. Error bars denote standard errors, and the red dashed line marks the fixed global classification diameter at $D = 195$ km.

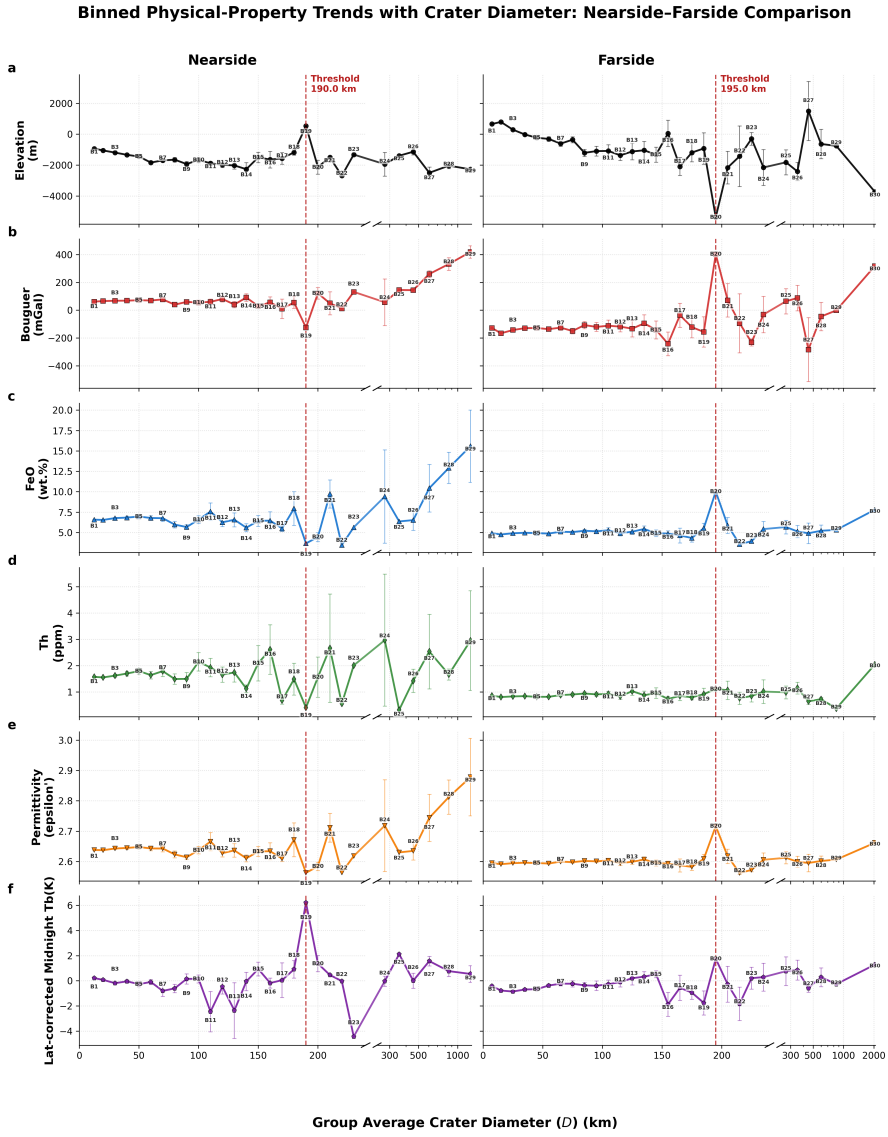


Figure 2: Diameter-binned means of six physical variables for the nearside and farside crater populations. (a) Topographic elevation; (b) Bouguer gravity anomaly; (c) FeO abundance; (d) Th abundance; (e) real part of the effective complex permittivity; and (f) latitude-corrected midnight microwave brightness temperature. The farside uses the original bins listed in Supplementary Table 1, whereas the nearside bins are shifted by 5 km. Error bars denote standard errors, and the red dashed lines mark the nearside transition diameter at $D = 190$ km and the farside transition diameter at $D = 195$ km.

Table 1: PCA-weighted Monte Carlo changepoint results for an upper search limit of 240 km

Region	Dominant bin	Bin range (km)	Bin midpoint (km)	Support probability	95% CI (km)
Global	B20	$190 \leq D < 200$	195	0.826	165–205
Nearside	B19	$185 \leq D < 195$	190	0.618	150–200
Farside	B20	$190 \leq D < 200$	195	0.913	185–195

Note: The values combine PCA-weighted segmented regression and Fisher optimal partitioning after Monte Carlo uncertainty propagation. Each transition diameter is expressed as the dominant bin midpoint and half-width. Support probability is the fraction of resampled changepoints that fall within the corresponding dominant bin. The result therefore represents a population-level transition scale rather than a direct morphological boundary.

2.2. Radial physical-property differences among four classes of impact structures

Stacked normalized radial profiles for the 6973 craters with diameters greater than 20 km show gradual variations for both nearside and farside impact craters. No pronounced annular differentiation in Bouguer gravity, topography, or elemental abundance occurs between $0.0R$ and $4.0R$. The mechanical, compositional-magnetic, and thermal-dielectric profiles are shown in Figs. 6, 7, and 8, respectively.

2.2.1. Deep basin response and hemispheric mechanical differentiation

Large impact basins exhibit more pronounced hemispheric differences. Nearside basins have strong positive central Bouguer anomalies and generally subdued topography, whereas farside basins show greater topographic relief, weaker positive central gravity anomalies, and an annular gravity low outside the crater rim (Fig. 6).

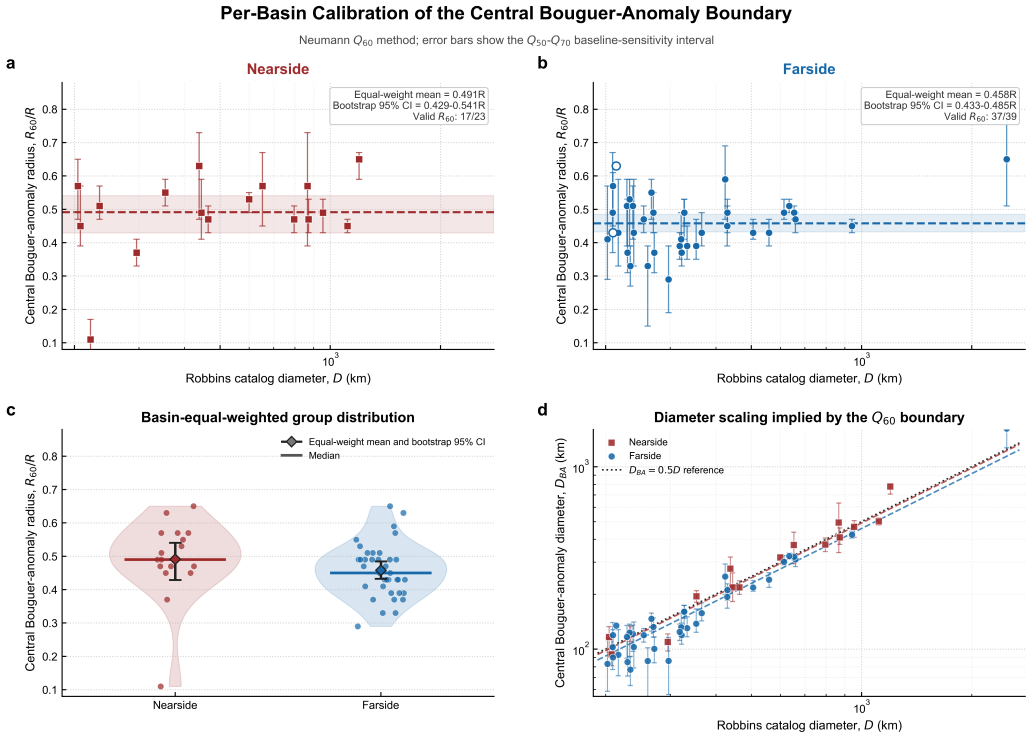


Figure 3: Basin-level central Bouguer-anomaly radii calibrated using the Neumann 60% quantile method; error bars denote R_{50}–R_{70} ranges. (a) Relationship between R_{60} and main-ring diameter for nearside basins; (b) relationship for farside basins; (c) equal-weight nearside and farside distributions, means, and bootstrap 95% confidence intervals; and (d) scaling between central Bouguer-anomaly diameter D_{BA} and main-ring diameter D. The black dashed line denotes $D_{\mathrm{BA}} = 0.5D$.

The basin-by-basin 60% quantile calibration yields valid R_{60} values for 17 of 23 nearside basins and 37 of 39 farside basins. Equal-weight basin means give $R_{\rm pr} = 0.458R$ for the farside, with a bootstrap 95% confidence interval of $0.433R$–$0.485R$, and $R_{\rm pr} = 0.491R$ for the nearside, with an interval of $0.429R$–$0.541R$. Basin-level values and the R_{50}–R_{70} sensitivity ranges are listed in Supplementary Table 4.

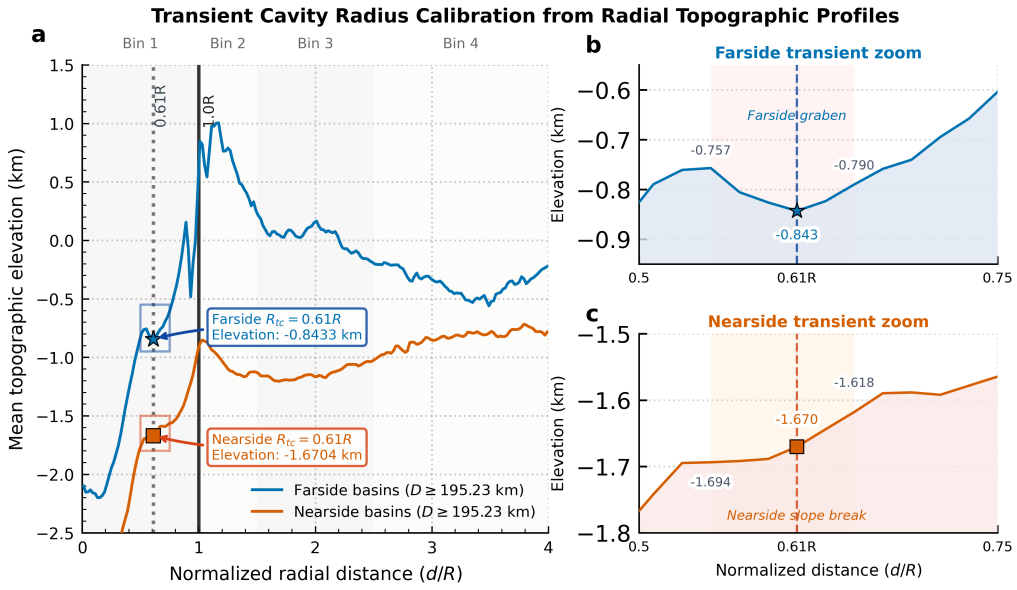


Figure 4: Normalized radial elevation profiles and calibration of the characteristic geophysical proxy near $0.61R$ for nearside and farside large impact basins. (a) Comparison of the hemispheric elevation profiles; (b) enlarged farside profile near $0.61R$; and (c) enlarged nearside profile near $0.61R$. The farside profile contains a trough near $0.61R$, whereas the nearside profile shows a break in slope that is consistent with later basaltic infilling.

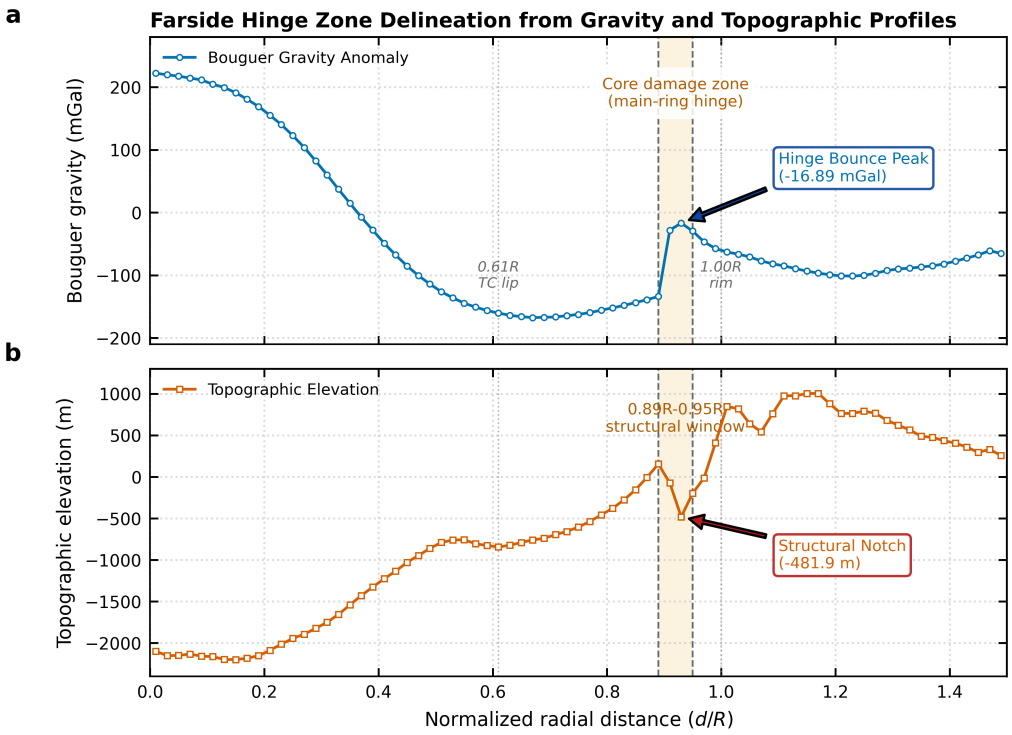


Figure 5: Coincident gravity and topographic signatures across the $0.89R$–$0.95R$ geophysical characteristic transition zone in farside large impact basins. (a) Normalized radial Bouguer gravity-anomaly profile and (b) normalized radial topographic-elevation profile. Calibrated from farside basins, this interval is interpreted as a main hinge-fault-zone proxy in the cold, mechanically strong highlands.

The nearside-farside comparison of the topographic feature near the inferred transient-cavity radius is shown in Fig. 4. Coincident gravity and topographic transitions across the main hinge-fault zone of farside large impact basins are shown in Fig. 5; the geological implications of both characteristic radii are considered below.

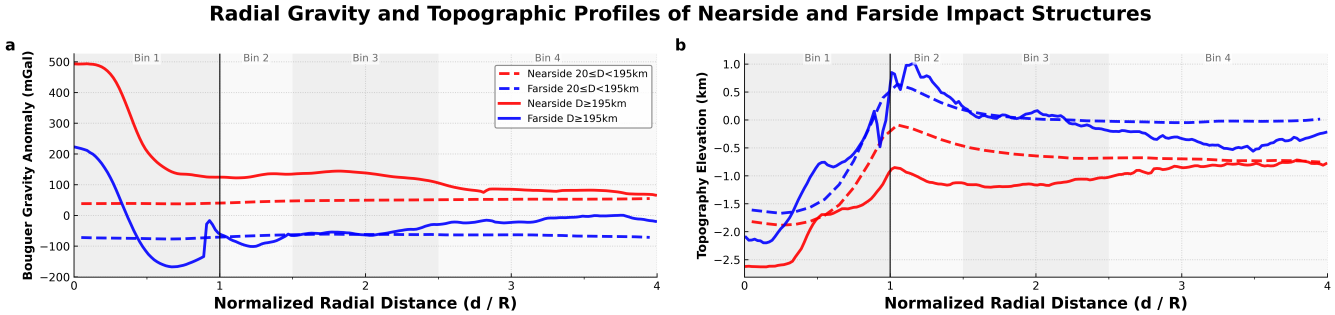


Figure 6: Stacked normalized radial profiles of gravity and topography. (a) Bouguer gravity anomaly and (b) topographic elevation. The horizontal axis is normalized radius from the basin center. Solid lines denote large impact basins and dashed lines denote impact craters; red indicates the nearside and blue the farside.

2.2.2. Impact excavation, magmatic infilling, and hemispheric compositional differentiation

The compositional profiles show that Th, K, and U abundances in nearside basins are elevated near the crater rim and in the proximal ejecta region, with maxima near $1R$, whereas FeO and TiO_2 abundances are higher in the basin interior (Fig. 7). In farside basins, Th, K, U, FeO, and TiO_2 abundances are generally low within the basin and near the rim, begin to increase gradually near Bin 2, and approach global mean values near Bin 3. Magnetic anomalies are generally stronger in farside than in nearside basins and show larger oscillations near the main hinge-fault zone calibrated from the farside population.

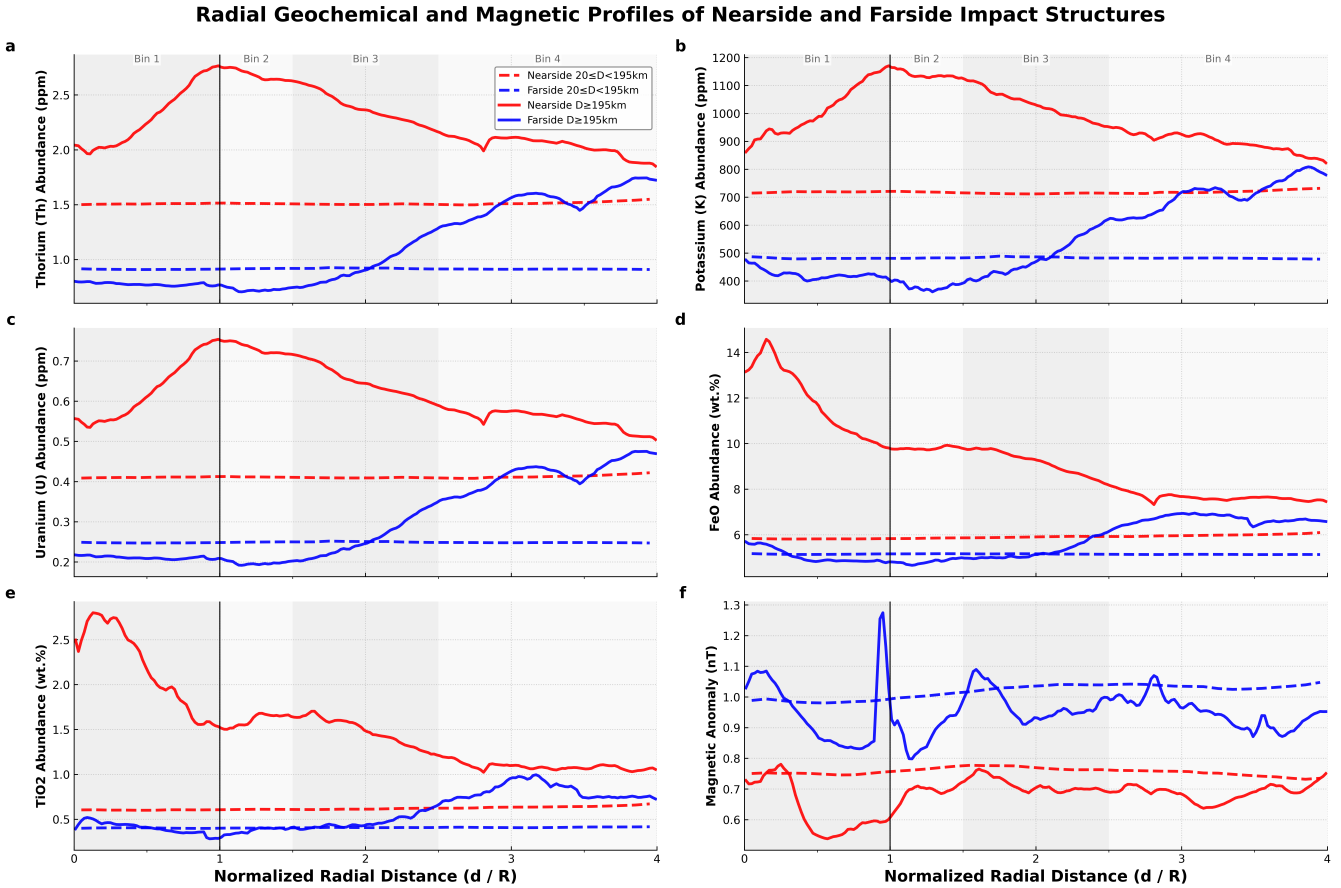


Figure 7: Stacked normalized radial profiles of elemental abundances and magnetic anomaly. (a) Th abundance; (b) K abundance; (c) U abundance; (d) FeO abundance; (e) TiO_2 abundance; and (f) magnetic anomaly. The horizontal axis is normalized radius from the basin center. Solid lines denote large impact basins and dashed lines denote impact craters; red indicates the nearside and blue the farside.

2.2.3. Mechanistic interpretation of microwave brightness temperature and permittivity

The thermal and dielectric profiles also differ between the two basin populations. Permittivity and brightness-temperature curves vary more strongly within nearside basins, and noon and midnight brightness temperatures show a local phase contrast near the crater rim (Fig. 8). Noon and midnight profiles for farside basins follow similar trends, although the midnight profile has a larger amplitude.

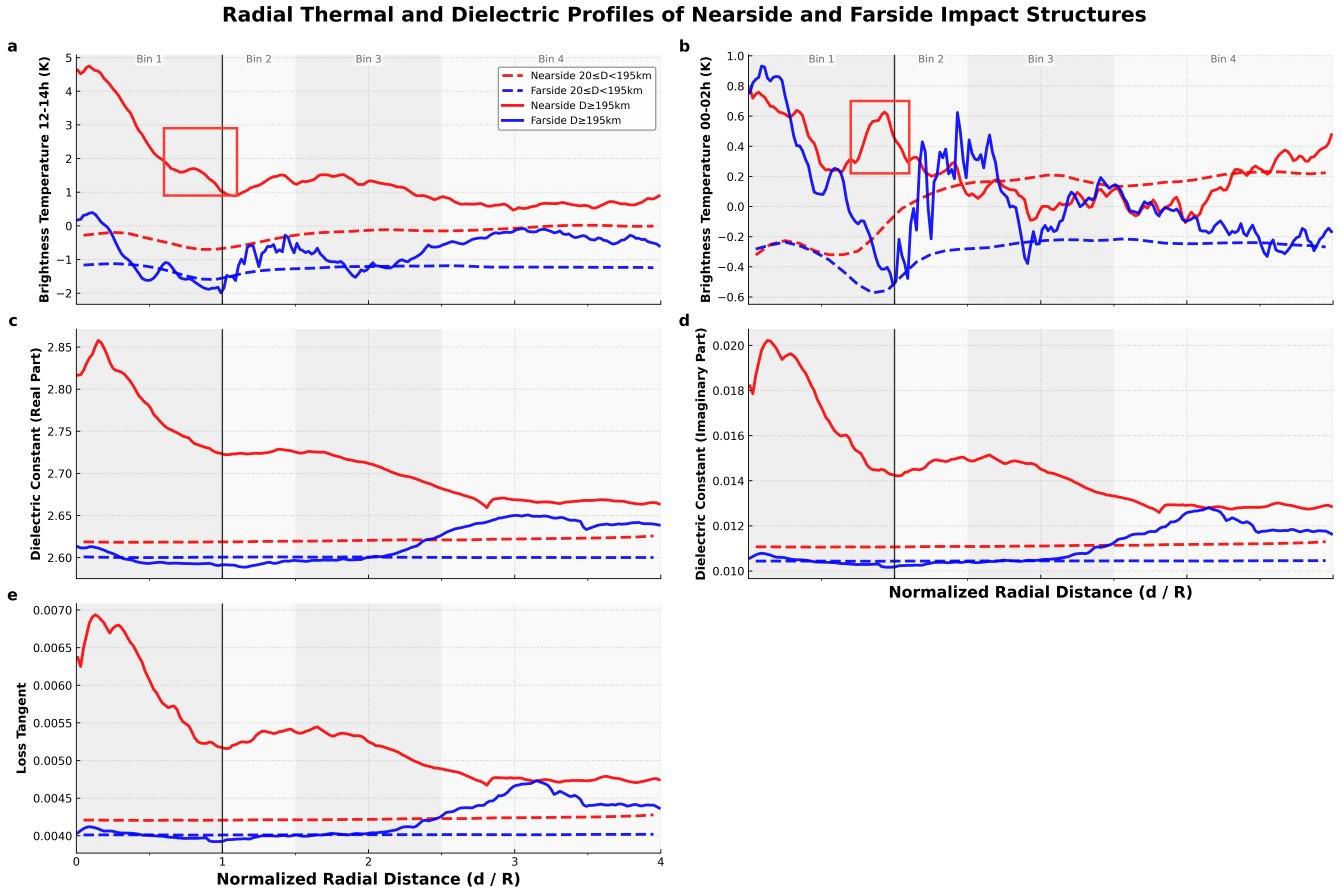


Figure 8: Stacked normalized radial profiles of brightness temperature and effective complex permittivity. (a) Latitude-corrected noon brightness temperature; (b) latitude-corrected midnight brightness temperature; (c) real part of the effective complex permittivity; (d) imaginary part of the effective complex permittivity; and (e) dielectric loss tangent. The horizontal axis is normalized radius from the basin center. Solid lines denote large impact basins and dashed lines denote impact craters; red indicates the nearside and blue the farside. The red boxes mark the radial intervals in which the noon and midnight brightness temperatures exhibit a local phase reversal.

3. Discussion

The six global physical variables change from gradual trends to larger bin-to-bin variability near $D = 195 \pm 5$ km, and the variability persists across several bins beyond B20 rather than forming an isolated extremum (Fig. 1 and Table 1). Morphological power-law relationships resolved by LOLA and saturation of the gravity response observed by GRAIL both indicate that smaller impact craters generally follow continuous scaling relations (Kalynn et al., 2013; Soderblom et al., 2015). Segmented regression, Fisher optimal partitioning, and Monte Carlo uncertainty propagation identify B20 as the dominant bin, with a support probability of 0.826. This agreement across methods and physical variables allows a population-level transition to be resolved even though some individual large-diameter bins contain few craters. We therefore interpret 195±5 km as a multisource geophysical transition scale rather than a sharp natural boundary or a replacement for morphological classification.

Below this scale, the limited variability is consistent with excavation, brecciation, and crater-wall adjustment mainly within the upper lunar crust. With increasing impact size, melt volume grows nonlinearly and the central structure evolves from a central peak to a peak ring (Cintala and Grieve, 1998; Baker et al., 2011); the gravity response may also become increasingly influenced by mantle uplift rather than porosity modification alone. Previous observations place the transition at 218 ± 17 km, numerical models span 140–215 km, and GRAIL results likewise indicate a scale near 200 km (Milbury et al., 2015; Neumann et al., 2015). The 195 ± 5 km scale is therefore consistent with independent morphological and gravity constraints, while adding

compositional, dielectric, and thermal evidence for a transition from shallow cratering response to deeper basin-scale response.

The hemispheric analysis gives 195 ± 5 km for the farside and 190 ± 5 km for the nearside, with support probabilities of 0.913 and 0.618, respectively (Fig. 2). Heat-producing elements in the PKT maintain a warmer, weaker nearside crust (Wieczorek and Phillips, 2000), and numerical models show that an otherwise equivalent impact can produce a larger final basin structure in the nearside crust (Miljković et al., 2013). The approximately 5 km lower nearside estimate is consistent with this tendency and may reflect the influence of thermal state. Subsequent classification and stacked normalized radial-profile analyses use 195 km as a fixed operational diameter, whereas 195 ± 5 km expresses the bin-scale precision of the characteristic transition scale.

Nearside large impact basins combine strong gravity anomalies with subdued topography (Fig. 6). Serenitatis basin, for example, has a pronounced central Bouguer gravity anomaly, whereas its topography is comparatively smooth (Supplementary Fig. 2). This gravity-topography decoupling is consistent with post-impact rebound of dense material beneath the basin and subsequent long-term viscoelastic adjustment of the surface as high nearside heat flow reduces the effective elastic thickness of the lithosphere (Jolliff et al., 2000; Dombard et al., 2013; Freed et al., 2014). Later FeO- and TiO_2-rich basaltic infilling could further smooth the topography without fully removing the deeper mass anomaly.

Basin-level calibrations are shown in Fig. 3. Panels (a) and (b) give R_{60} for nearside and farside basins, respectively, with error bars denoting the R_{50}–R_{70}

sensitivity ranges; panel (c) shows the equal-weight basin distributions and bootstrap intervals of their means. When normalized by the main-ring (MR) radius R, the equal-weight mean R_{pr} values are $0.458R$ for the farside and $0.491R$ for the nearside. The confidence intervals overlap and therefore do not support a statistically significant hemispheric difference in peak-ring radius. Figure 3d further shows an approximately linear increase in central Bouguer-anomaly diameter with Robbins main-ring diameter. Mean nearside and farside ratios are approximately 0.491 and 0.458, respectively, both close to the reference relation $D_{\mathrm{BA}} = 0.5D$. The basin-level values remain dispersed, suggesting that mascon setting, basaltic infilling, and structural preservation affect the local position of the Bouguer transition.

Farside large impact basins preserve clearer tectonic annuli, as illustrated by Hertzsprung basin (Supplementary Fig. 3). The normalized radial profiles contain a topographic minimum near $0.61R$ that is used here as a geophysical proxy for the transient-cavity collapse zone; its hemispheric expression is compared in Fig. 4 and Supplementary Table 5. During the modification stage, cold, mechanically strong outer crustal blocks can slump inward along normal faults, and greater farside lithospheric rigidity may preserve this graben-like topographic feature (Baker et al., 2011; Milbury et al., 2015; Zhang et al., 2024). Between $0.89R$ and $0.95R$ in farside large impact basins, a local gravity high coincides with a topographic depression. This juxtaposition may reflect superposition of a shallow tectonic feature and a deeper annular mass anomaly near the main hinge-fault zone. The radius range was calibrated from farside basins and is treated as a geophysical characteristic transition zone, not as a directly observed fault boundary (Fig. 5 and Supple-

mentary Table 6). For nearside basins, it provides a reference radius against which thermal modification and basaltic infilling can be compared. This interpretation is consistent with shear-stress concentration and transition from the collapsed basin interior to the outer crustal root (Wieczorek and Phillips, 1998; Zuber et al., 2016; Neumann et al., 2015).

The compositional structure of nearside basins is consistent with a distinct sequence of modification. Th, K, and U are enriched outside the crater rim in the global profiles (Fig. 7) and in Serenitatis basin (Supplementary Fig. 4). This distribution supports excavation or redistribution of KREEP-rich material from the deep or middle-to-lower lunar crust into the proximal ejecta region (Jolliff et al., 2000; McGetchin et al., 1973). FeO and TiO_2 are instead enriched within the basin interior, consistent with later emplacement of FeO- and TiO_2-rich mare basalt along structural pathways and subsequent infilling of the basin floor (Pieters et al., 2001). The spatial separation between outer heat-producing elements and centrally concentrated basaltic components supports a sequence of excavation and ejecta emplacement followed by magmatic infilling, although local pre-impact compositional heterogeneity may also contribute.

Farside basins are generally depleted in KREEP-rich material and oxides within their interiors and lack extensive late-stage basaltic coverage. Their physical-property patterns therefore appear less modified by mare infilling than comparable nearside basins. The Th and FeO distributions and normalized radial profiles of Hertzsprung basin are shown in Supplementary Fig. 5. Local Th enrichment at the basin center may be related to differentiation during cooling of the impact-melt pool. The outward transition to

low FeO and low Th may reflect exposure of deep purest anorthosite after removal of the surficial mixed breccia (Korotev et al., 2003; Cintala and Grieve, 1998). Local enhancement of magnetic anomalies near the main hinge-fault zone may record remanent magnetization acquired as the impact melt sheet cooled through the Curie temperature, although later secondary impacts and ejecta overprinting can make this signal discontinuous.

Latitude-corrected microwave brightness temperature and effective complex permittivity jointly reflect the density, porosity, composition, and thermal inertia of the lunar regolith. FeO- and TiO_2-rich basalts within nearside basins increase electromagnetic loss and reduce microwave penetration depth, making noon brightness temperature more sensitive to the shallow sun-heated layer (Fa and Jin, 2007; Fa et al., 2011; Fa, 2023). Faults near the reference main hinge-fault radius may have provided pathways for mafic intrusions or volcanic infilling (Fig. 8). Dense rock bodies heat and cool slowly, producing relatively low temperatures at noon and relatively high temperatures at midnight. Such a day-night phase reversal is consistent with late thermal modification of nearside basins. In Serenitatis basin, the joint thermal-dielectric relationships are shown in Supplementary Fig. 6. High FeO and TiO_2 abundances increase the dielectric loss tangent and reduce the penetration depth of 7.8 GHz microwaves. The resulting contrast between shallow daytime heating and the slower nighttime cooling of high-thermal-inertia material produces a pronounced day-night brightness-temperature phase reversal near the reference main hinge-fault radius.

Brightness-temperature variations in farside basins may reflect differences in structural thermal inertia, as illustrated by the thermal-dielectric response

of the global profiles (Fig. 8) and Hertzsprung basin (Supplementary Fig. 7). The greater microwave penetration depth could allow dense rocks formed by slow cooling of the central impact-melt pool to continue releasing heat toward the surface at night, producing a relatively high midnight brightness temperature. The low-FeO, low-TiO_2 anorthositic core has low dielectric loss and corresponds to low permittivity and loss-tangent values. Toward $0.61R$ and the main hinge-fault zone, changes in brecciation, fault-network density, and debris compaction are accompanied by gradual increases in the real and imaginary parts of the permittivity and in the dielectric loss tangent. The hemispheric thermal contrast therefore suggests that nearside basins are more strongly influenced by thermal-inertia differences associated with composition and magmatism, whereas farside basins may retain a stronger signal of primary structure and fragmentation.

The characteristic transition scale of 195 ± 5 km supports the interpretation that impact structures begin to exhibit a more persistent deeper geophysical response near this scale (Fig. 1). When a fixed 195 km classification diameter is applied for population stacking, nearside and farside large impact basins retain distinct gravity, topographic, compositional, and thermophysical structures. This result is consistent with previous constraints from lunar crustal terranes, GRAIL crustal thickness, and the preservation state of farside large impact basins: the nearside is enriched in heat-producing elements and mare basalts, whereas the farside preserves a cold, thick crust and feldspathic highlands (Jolliff et al., 2000; Wieczorek et al., 2013; Trowbridge et al., 2020; Zhang et al., 2024).

Large impacts thus occurred in nearside and farside targets with pre-

existing thermomechanical and compositional differences and subsequently sampled and modified this dichotomy. Higher heat flow and more extensive basaltic activity in nearside basins likely promoted viscoelastic relaxation, mascon development or preservation, and volcanic infilling. Farside basins experienced less thermal modification and may therefore preserve clearer topographic and geophysical signatures of collapse-related structures and anorthositic crust. These differences provide a reference for understanding how asymmetric structures on early terrestrial bodies are preserved and reworked by later impacts and thermal evolution.

Diameter binning and stacked normalized radial profiles derived from the 32 ppd global lunar physical-property grid and crater database yield the following conclusions:

1. A multisource geophysical transition scale between global impact craters and basins is centered at $D = 195 \pm 5$ km, with a support probability of 0.826. Farside and nearside transition scales are 195 ± 5 km and 190 ± 5 km, with support probabilities of 0.913 and 0.618, respectively. This scale is a population-level geophysical transition and does not redefine the traditional morphological classification boundary.
2. Normalized radial physical-property profiles vary gradually for both nearside and farside impact craters, whereas large impact basins exhibit pronounced hemispheric differentiation.
3. With the main-ring (MR) radius R as the normalization scale, the basin-level 60% quantile method applied to the Bouguer anomaly gives peak-ring (PR) radii of $R_{\mathrm{pr}} = 0.46R$ for the farside and $R_{\mathrm{pr}} = 0.49R$ for the nearside. The two confidence intervals overlap.

4. A characteristic topographic radius interpreted as a transient-cavity-collapse proxy is centered near $0.61R$. A geophysical characteristic transition zone calibrated from farside large impact basins falls within $0.89R$–$0.95R$ and serves as a main hinge-fault-zone proxy. These radii provide reference scales for comparing nearside and farside basin modification rather than directly observed geological boundaries.
5. Nearside basins record outward enrichment of KREEP-rich material and infilling by FeO- and TiO_2-rich mare basalt. A day-night brightness-temperature phase reversal near the main hinge-fault radius is consistent with mafic bodies with high thermal inertia. Farside basins retain signatures consistent with impact-melt-pool differentiation, purest-anorthosite cores, and cold, mechanically strong highland crust.
6. The contrasting physical structures and modification histories of nearside and farside large impact basins indicate that large impacts occurred in targets with pre-existing thermomechanical and compositional differences and subsequently sampled and modified this lunar hemispheric dichotomy.

Further work combining alternative crater catalogs, GRAIL crustal-thickness data, and numerical impact models is required to test the relationship between the approximately 190–200 km characteristic scale, transient excavation, Moho disturbance, and peak-ring formation. Multi-frequency microwave, radar, and thermal-infrared observations may further distinguish pre-impact crustal properties from post-impact volcanic infilling and thermal relaxation.

4. Methods

4.1. Multi-source datasets and common grid

The physical-property datasets comprise topographic elevation measured by the Lunar Orbiter Laser Altimeter (LOLA) onboard the Lunar Reconnaissance Orbiter (LRO); Bouguer gravity anomaly derived from the Gravity Recovery and Interior Laboratory (GRAIL) mission; magnetic anomaly measured by the SElenological and ENgineering Explorer (SELENE); K, Th, U, FeO, and TiO_2 abundances from the Gamma-Ray Spectrometer (GRS) onboard Lunar Prospector (LP); and noon (12:00–14:00) and midnight (00:00–02:00) brightness temperatures at 7.8 GHz from the Microwave Radiometer (MRM) onboard Chang'E-2 (CE-2). Crater locations and diameters were obtained from the Robbins global lunar crater database (Robbins, 2019). Because the datasets differ in spatial resolution, projection, and sampling interval, they were resampled to a common 32 ppd latitude-longitude grid, corresponding to a pixel scale of approximately 0.95 km at the equator. This resolution supports annular statistics for craters larger than 20 km in diameter. The principal global data layers are shown in Supplementary Fig. 1.

The Bouguer gravity anomaly was calculated from the GRAIL spherical harmonic model truncated at degree 800, and topography was obtained from the original 64 ppd LOLA product. Each LOLA grid value represents the radial distance r_{LOLA} from the lunar center. Using $R_0 = 1737.4$ km as the lunar reference radius, topographic elevation relative to the reference sphere was calculated as

$$H = r_{\mathrm{LOLA}} - R_0 \tag{1}$$

This elevation was used in all subsequent diameter-binned statistics and normalized radial profiles and was downsampled from 64 to 32 ppd by bilinear interpolation. Magnetic anomalies were taken from the SELENE global magnetic-field product at 30 km altitude and resampled by nearest-neighbor interpolation to preserve the original values as closely as possible (Tsunakawa et al., 2014). We used latitude-corrected CE-2 MRM brightness temperatures at 7.8 GHz. The midnight observations are less affected by solar heating and are therefore better suited to characterizing subsurface thermal inertia and rock density. The radioactive-element and oxide-abundance products have an original spatial resolution of 2° and were also resampled by nearest-neighbor interpolation.

Crater geometry was taken from the Robbins database. We first selected 83 061 craters with $D \geq 5$ km for the size-spectrum analysis, and then selected 6973 craters with $D \geq 20$ km for the stacked normalized radial-profile analysis. The lunar nearside was defined by longitudes 270°–360° and 0°–90°, and the lunar farside by 90°–270°. For the subsequent population stacking, the sample was divided at the fixed 195 km classification diameter into nearside large impact basins, farside large impact basins, nearside impact craters, and farside impact craters.

4.2. Inversion of complex permittivity

The effective complex permittivity of the lunar regolith was calculated from empirical relationships and Maxwell-Garnett mixing theory (Fa et al., 2011; Fa and Wieczorek, 2012; Fa, 2023). The grain density G depends on FeO and TiO_2 abundance:

$$G = 0.0273\,\mathrm{FeO} + 0.011\,\mathrm{TiO_2} + 2.773. \quad (2)$$

For a prescribed mean porosity ϕ, the bulk density is

$$\rho_b = G(1 - \phi). \tag{3}$$

At the reference density $\rho_{\text{ref}} = 1.7$ g/cm^3, the reference real permittivity and dielectric loss tangent are

$$\begin{aligned} \epsilon'_{\text{ref}} &= 2.75, \\ \log_{10}(\tan\delta_{\text{ref}}) &= -2.395 + 0.064\,\text{TiO}_2. \end{aligned} \tag{4}$$

The lunar regolith was approximated as a multiphase mixture of vacuum-filled pores and solid mineral grains, with a vacuum-host permittivity $\epsilon_h = 1$ and a solid-grain permittivity ϵ_s (Fa, 2023). Under the Maxwell-Garnett mixing model, the effective complex permittivity ϵ satisfies

$$\frac{\epsilon - 1}{\epsilon + 2} = f\,\frac{\epsilon_s - 1}{\epsilon_s + 2}, \qquad f = 1 - \phi = \frac{\rho_b}{G}. \tag{5}$$

Normalizing by the actual bulk density gives a constant C that depends only on the dielectric properties and grain density of the solid material (Fa and Wieczorek, 2012):

$$\frac{\epsilon - 1}{\rho_b(\epsilon + 2)} = \frac{\epsilon_s - 1}{G(\epsilon_s + 2)} = C. \tag{6}$$

Let $\epsilon_{\text{ref}} = \epsilon'_{\text{ref}} + i\epsilon''_{\text{ref}}$. Calibrating C at the reference state and solving for ϵ gives

$$\begin{aligned} C &= \frac{\epsilon_{\text{ref}} - 1}{\rho_{\text{ref}}(\epsilon_{\text{ref}} + 2)}, \\ \epsilon &= \frac{1 + 2\rho_b C}{1 - \rho_b C}. \end{aligned} \tag{7}$$

This procedure yields the effective complex permittivity $\epsilon = \epsilon' + i\epsilon''$ and dielectric loss tangent $\tan\delta = \epsilon''/\epsilon'$ for each grid cell. The model links FeO and TiO_2 abundance and porosity to electromagnetic loss, providing a basis

for interpreting the coupling between microwave brightness temperature and basin composition (Kobayashi et al., 2023). The inversion workflow is shown in Supplementary Fig. 8.

4.3. Diameter binning and changepoint detection

Diameter binning was used to characterize changes in the physical fields with crater diameter. Several of the compositional, brightness-temperature, and permittivity layers are strongly correlated, and including all 13 layers in the changepoint analysis would repeatedly represent similar information. We therefore selected six comparatively independent variables that represent morphology, gravity, composition, dielectric properties, and thermal state: topographic elevation, Bouguer gravity anomaly, FeO abundance, Th abundance, real part of permittivity, and latitude-corrected midnight microwave brightness temperature (Fig. 1). Craters were assigned to bins B1–B31 as listed in Supplementary Table 1, and each transition diameter was defined by the midpoint of the selected bin. This diameter is a statistical classification scale used for population analysis and is distinct from a morphological class boundary. The search was restricted to $D < 240$ km because the transition from complex craters to peak-ring basins occurs primarily near 200 km, whereas larger multi-ring basins are additionally affected by crust-mantle coupling, impact melting, and long-term thermal relaxation (Pike, 1980; Melosh and McKinnon, 1978; Baker et al., 2011; Melosh, 1980; Cintala and Grieve, 1998).

The transition scale was jointly estimated from the six standardized variables. PCA-weighted segmented regression and Fisher optimal partitioning were applied independently to the global, nearside, and farside samples. We

then perturbed the bin means according to their standard errors in a Monte Carlo uncertainty-propagation procedure, repeated the changepoint detection for each realization, and calculated the support probability for each interval. This framework treats the transition as a coherent change in a multivariate population rather than as a property of one sparsely populated diameter bin. Individual large-diameter bins contain few craters, but their influence is moderated by standard-error propagation, by requiring agreement between two changepoint methods, and by testing whether the same bin remains favored after bin shifts and changes in the upper search limit. A standard error cannot be calculated for a bin containing a single sample; such values were replaced by the median standard error of valid $D \geq 240$ km bins within the corresponding spatial domain. If no such bin was available, the median standard error of all valid bins for that variable was used.

For the sensitivity analysis, the three sets of bin boundaries were shifted successively by 1–5 km, and missing standard errors were replaced by the minimum, median, or maximum standard error among valid $D \geq 240$ km bins. Each configuration was sampled 1000 times with the same random seed; the results are listed in Supplementary Table 2. We also extended the upper search limit progressively from 240 to 2600 km and repeated the procedure. The nearside analysis used bins shifted by 5 km and an upper limit increased by the same amount; the results are provided in Supplementary Table 3.

4.4. Stacked normalized radial-profile analysis

The stacked normalized radial-profile analysis used all 13 data layers. Diameter D in the Robbins database was treated as the main-ring (MR) diameter. The great-circle distance d between each grid cell and the center

of an impact structure was normalized by $R = D/2$, such that $r' = d/R$ and $r' = 1$ corresponds to the main-ring boundary. Profiles extended from $0.0R$ to $4.0R$ and were divided into the basin interior ($0.0R$–$1.0R$), crater-rim collapse zone ($1.0R$–$1.5R$), continuous proximal ejecta blanket ($1.5R$–$2.5R$), and distal background region ($2.5R$–$4.0R$) (Pike, 1980; McGetchin et al., 1973; Xiao et al., 2021; Zhang et al., 2023; Wahl et al., 2020).

For each impact structure, this radial range was divided into concentric annuli. Annular widths of $0.02R$ for large impact basins and $0.10R$ for impact craters balanced scale coverage against radial-profile detail. For a physical variable X, the azimuthal mean in annulus $A_{i,j}$ for the ith crater is

$$\overline{X}_{i,j} = \frac{1}{N_{i,j}} \sum_{p \in A_{i,j}} X_p, \tag{8}$$

where p denotes a grid cell within the annulus and $N_{i,j}$ is the number of valid cells.

For population stacking, the sample was divided by the fixed 195 km classification diameter and lunar hemisphere into nearside large impact basins, farside large impact basins, nearside impact craters, and farside impact craters. Within each category, the azimuthal means of individual objects at the same normalized radius were then averaged:

$$\overline{X}_j^{\text{group}} = \frac{1}{M_j} \sum_{i=1}^{M_j} \overline{X}_{i,j}, \tag{9}$$

where M_j is the number of impact structures with valid values in the jth annulus. Calculating the azimuthal mean for each object before averaging among objects assigns equal weight to every impact structure in the population profile. The stacked azimuthal means were plotted against normalized radius to obtain profiles for the four categories across all 13 data layers.

4.5. Calibration of characteristic radii

Characteristic radii of large impact basins are expressed in the normalized coordinate d/R, where R is the main-ring (MR) radius and the peak-ring (PR) radius is R_{pr}. For multi-ring basins, the innermost ring can be treated as the peak ring (Neumann et al., 2015). Following Neumann et al. (Neumann et al., 2015), we determined the peak-ring radius separately for each basin with $D \geq 195$ km. The 60% quantile of all valid Bouguer anomalies within the main ring ($d/R \leq 1$) was first used as a baseline, and the normalized radial profile of the Bouguer gravity anomaly was then calculated. The first outward decrease of the profile to this baseline defined R_{60}, which was assigned to the final radial sample above the baseline before the crossing, at a sampling interval of $0.02R$. The procedure was repeated using 50% and 70% quantile baselines, and R_{50}–R_{70} defines the calibration range. A basin was recorded as not detected if the central annulus was already below the baseline or if no downward crossing occurred within $1.5R$. Valid nearside and farside basins were averaged with equal weight. We resampled complete basins 10 000 times to obtain bootstrap 95% confidence intervals for the mean, preventing large basins with more grid cells from dominating the population statistics.

A transient-cavity-related characteristic radius was estimated from topographic relief in the normalized radial profiles. Numerical models define the transient crater by the radial extent of the excavation cavity at its maximum volume and show that estimating transient-crater size for large basins from an empirical fraction of the final rim introduces substantial uncertainty (Potter et al., 2012). Cavity collapse can also produce normal-fault-like structures

outside the cavity, expressed at the surface as annular troughs or breaks in slope (Potter, 2015). We therefore calculated normalized radial elevation profiles and first differences separately for nearside and farside large impact basins. The characteristic radius was calibrated from a persistent local topographic minimum and the adjacent break in slope, without prescribing its ratio to the final crater rim.

The main hinge-fault zone was calibrated using a geophysical potential-field criterion, with its location defined by coincident transitions in the normalized radial profiles of Bouguer gravity anomaly and topography. Because farside basins better preserve their tectonic structure, the calibration used the farside population; nearside basins were retained only for comparison, and local derivatives provided supporting criteria.

Data availability

The LRO/LOLA GDR topography and GRAIL LGRS RDR gravity data used in this study are available at `https://pds-geosciences.wustl.edu/missions/lro/lola.htm` and `https://pds-geosciences.wustl.edu/missions/grail/default.htm`, respectively. The SELENE (Kaguya) LMAG lunar magnetic-anomaly grid is available at `https://darts.isas.jaxa.jp/missions/kaguya`. Lunar Prospector GRS K, Th, U, FeO, and TiO_2 abundance data are available at `https://pds-geosciences.wustl.edu/missions/lunarp/grs_elem_abundance.html`. Chang'E-2 MRM noon and midnight brightness temperatures at 7.8 GHz are available at `https://pds-geosciences.wustl.edu/missions/chang'e/index.htm`. The Robbins global lunar crater database is available at `https:`

//astrogeology.usgs.gov/search/map/moon_crater_database_v1_robbins. All source-data URLs were accessed on 6 August 2026. The large public source products are not redistributed in the accompanying archive; their exact product identifiers, versions, sources, and processing steps are documented in the archived data_sources.md file. Compact derived tables sufficient to inspect the reported statistics, redraw the principal profile plots, and verify the changepoint and basin-radius conclusions are publicly available with the reproducibility code and documentation in Zenodo (Ge et al., 2026) at https://doi.org/10.5281/zenodo.21817250.

Code availability

The analysis and upstream preprocessing scripts, parameter configuration, run order, software requirements, and software-version record are publicly archived with the derived data in Zenodo (Ge et al., 2026) at https://doi.org/10.5281/zenodo.21817250.

CRediT authorship contribution statement

Quanxi Ge: Conceptualization, Data curation, Formal analysis, Investigation, Methodology, Software, Visualization, Writing – original draft. Changbao Yang: Conceptualization, Methodology, Supervision, Writing – review & editing. Liguo Han: Methodology, Writing – review & editing. Lezhen Han: Investigation. Shiqin Yang: Investigation. Yu He: Validation. Jiawen Chen: Validation.

Funding

This work was supported by the National Natural Science Foundation of China [grant numbers 42130805 and 42074154]. The funding source had no involvement in the study design; in the collection, analysis, or interpretation of data; in the writing of the manuscript; or in the decision to submit the article for publication.

Competing interests

The authors declare no competing interests.

Declaration of generative AI and AI-assisted technologies in the manuscript preparation process

During the preparation of this work the authors used ChatGPT (OpenAI) in order to format the manuscript using the Elsevier LaTeX template. After using this service, the authors reviewed and edited the content as needed and take full responsibility for the content of the published article.

References

Baker, D.M.H., Head, J.W., Fassett, C.I., Kadish, S.J., Smith, D.E., Zuber, M.T., Neumann, G.A., 2011. The transition from complex crater to peak-ring basin on the Moon: New observations from the Lunar Orbiter Laser Altimeter (LOLA) instrument. Icarus 214, 377–393. doi:10.1016/j.icarus.2011.05.030.

699 Cintala, M.J., Grieve, R.A.F., 1998. Scaling impact melting and crater di-
700 mensions: Implications for the lunar cratering record. Meteorit. Planet.
701 Sci. 33, 889–912. doi:10.1111/j.1945-5100.1998.tb01695.x.

702 Dombard, A.J., Hauck, S.A., Balcerski, J.A., 2013. On the origin of mascon
703 basins on the Moon (and beyond). Geophys. Res. Lett. 40, 28–32. doi:10
704 .1029/2012GL054310.

705 Fa, W., 2023. Overview of the dielectric permittivity of lunar surface mate-
706 rials and implications for Chang'E-5 sample measurements (in Chinese).
707 Sci. Sin.-Phys. Mech. Astron. 53, 239602. doi:10.1360/SSPMA-2022-0396.

708 Fa, W., Cai, Y., 2013. Circular polarization ratio characteristics of impact
709 craters from Mini-RF observations and implications for ice detection at
710 the polar regions of the Moon. J. Geophys. Res. Planets 118, 1582–1608.
711 doi:10.1002/jgre.20110.

712 Fa, W., Jin, Y.Q., 2007. Simulation of brightness temperature from lunar
713 surface and inversion of regolith-layer thickness. J. Geophys. Res. Planets
714 112, E05003. doi:10.1029/2006JE002751.

715 Fa, W., Jin, Y.Q., 2010. Analysis of microwave emission observations of the
716 lunar surface by Chang'E-1 and inversion of lunar regolith thickness (in
717 Chinese). Sci. Sin. Inf. 40, 115–127.

718 Fa, W., Wieczorek, M.A., 2012. Regolith thickness over the lunar nearside:
719 Results from Earth-based 70-cm Arecibo radar observations. Icarus 218,
720 771–787. doi:10.1016/j.icarus.2012.01.010.

721 Fa, W., Wieczorek, M.A., Heggy, E., 2011. Modeling polarimetric radar
722 scattering from the lunar surface: Study on the effect of physical properties
723 of the regolith layer. J. Geophys. Res. Planets 116, E03005. doi:10.1029/
724 2010JE003649.

725 Feng, J., Zou, Y., Bian, W., Zheng, Y., Li, C., 2010. Review on physical
726 models of lunar brightness temperature. Chin. J. Geochem. 29, 204–211.
727 doi:10.1007/s11631-010-0204-9.

728 Freed, A.M., Johnson, B.C., Blair, D.M., Melosh, H.J., Neumann, G.A.,
729 Phillips, R.J., Solomon, S.C., Wieczorek, M.A., Zuber, M.T., 2014. The
730 formation of lunar mascon basins from impact to contemporary form. J.
731 Geophys. Res. Planets 119, 2378–2397. doi:10.1002/2014JE004657.

732 Ge, Q., Yang, C., Han, L., Han, L., Yang, S., He, Y., Chen, J., 2026. [dataset]
733 EPSL lunar crater–basin derived dataset and reproducibility code. Zenodo.
734 URL: https://doi.org/10.5281/zenodo.21817250, doi:10.5281/zeno
735 do.21817250. version 1.0.

736 Heiken, G.H., Vaniman, D.T., French, B.M., 1991. Lunar Sourcebook: A
737 User's Guide to the Moon. Cambridge Univ. Press, Cambridge.

738 Jiang, Y., Xu, C., Chen, L., 2024. An overview and perspective of identifying
739 lunar craters. Sci. China Earth Sci. 67, 1395–1416. doi:10.1007/s11430
740 -023-1233-2.

741 Jolliff, B.L., Gillis, J.J., Haskin, L.A., Korotev, R.L., Wieczorek, M.A., 2000.
742 Major lunar crustal terranes: Surface expressions and crust-mantle origins.
743 J. Geophys. Res. Planets 105, 4197–4216. doi:10.1029/1999JE001103.

744 Kalynn, J., Johnson, C.L., Osinski, G.R., Barnouin, O., 2013. Topographic
745 characterization of lunar complex craters. Geophys. Res. Lett. 40, 38–42.
746 doi:10.1029/2012GL053608.

747 Kobayashi, M., Miyamoto, H., Pál, B.D., Niihara, T., Takemura, T., 2023.
748 Laboratory measurements show temperature-dependent permittivity of lu-
749 nar regolith simulants. Earth Planets Space 75, 8. doi:10.1186/s40623-0
750 22-01757-5.

751 Korotev, R.L., Jolliff, B.L., Zeigler, R.A., Gillis, J.J., Haskin, L.A., 2003.
752 Feldspathic lunar meteorites and their implications for compositional re-
753 mote sensing of the lunar surface and the composition of the lunar crust.
754 Geochim. Cosmochim. Acta 67, 4895–4923. doi:10.1016/j.gca.2003.0
755 8.001.

756 Lawrence, D.J., Elphic, R.C., Feldman, W.C., Prettyman, T.H., Gasnault,
757 O., Maurice, S., 2003. Small-area thorium features on the lunar surface.
758 J. Geophys. Res. Planets 108, 5102. doi:10.1029/2003JE002050.

759 McGetchin, T.R., Settle, M., Head, J.W., 1973. Radial thickness variation in
760 impact crater ejecta: Implications for lunar basin deposits. Earth Planet.
761 Sci. Lett. 20, 226–236. doi:10.1016/0012-821X(73)90162-3.

762 Melosh, H.J., 1980. Cratering mechanics—observational, experimental, and
763 theoretical. Annu. Rev. Earth Planet. Sci. 8, 65–93. doi:10.1146/annure
764 v.ea.08.050180.000433.

765 Melosh, H.J., 1989. Impact Cratering: A Geologic Process. Oxford Univ.
766 Press, New York.

Melosh, H.J., McKinnon, W.B., 1978. The mechanics of ringed basin formation. Geophys. Res. Lett. 5, 985–988. doi:10.1029/GL005i011p00985.

Milbury, C., Johnson, B., Melosh, H., Collins, G., Blair, D., Soderblom, J., Nimmo, F., Bierson, C., Phillips, R., Zuber, M., 2015. Preimpact porosity controls the gravity signature of lunar craters. Geophys. Res. Lett. 42, 9711–9716. doi:10.1002/2015GL066198.

Miljković, K., Wieczorek, M.A., Collins, G.S., Laneuville, M., Neumann, G.A., Melosh, H.J., Solomon, S.C., Phillips, R.J., Smith, D.E., Zuber, M.T., 2013. Asymmetric distribution of lunar impact basins caused by variations in target properties. Science 342, 724–726. doi:10.1126/science.1243224.

Neumann, G.A., Zuber, M.T., Wieczorek, M.A., Head, J.W., Baker, D.M., Solomon, S.C., Smith, D.E., Lemoine, F.G., Mazarico, E., Sabaka, T.J., et al., 2015. Lunar impact basins revealed by Gravity Recovery and Interior Laboratory measurements. Sci. Adv. 1, e1500852. doi:10.1126/sciadv.1500852.

Pieters, C.M., Head, III, J.W., Gaddis, L., Jolliff, B., Duke, M., 2001. Rock types of South Pole-Aitken basin and extent of basaltic volcanism. J. Geophys. Res. Planets 106, 28001–28022. doi:10.1029/2000JE001414.

Pike, R.J., 1980. Geometric Interpretation of Lunar Craters. Professional Paper 1046-C, U.S. Government Printing Office, Washington, D.C. doi:10.3133/pp1046C.

789 Potter, R.W.K., 2015. Investigating the onset of multi-ring impact basin
790 formation. Icarus 261, 91–99. doi:10.1016/j.icarus.2015.08.009.

791 Potter, R.W.K., Kring, D.A., Collins, G.S., Kiefer, W.S., McGovern, P.J.,
792 2012. Estimating transient crater size using the crustal annular bulge:
793 Insights from numerical modeling of lunar basin-scale impacts. Geophys.
794 Res. Lett. 39, L18203. doi:10.1029/2012GL052981.

795 Prettyman, T.H., Hagerty, J., Elphic, R., Feldman, W., Lawrence, D., McK-
796 inney, G., Vaniman, D., 2006. Elemental composition of the lunar surface:
797 Analysis of gamma ray spectroscopy data from Lunar Prospector. J. Geo-
798 phys. Res. Planets 111, E12007. doi:10.1029/2005JE002656.

799 Robbins, S.J., 2019. A new global database of lunar impact craters > 1–2
800 km: 1. Crater locations and sizes, comparisons with published databases,
801 and global analysis. J. Geophys. Res. Planets 124, 871–892. doi:10.1029/
802 2018JE005592.

803 Shkuratov, Y.G., Bondarenko, N.V., 2001. Regolith layer thickness mapping
804 of the Moon by radar and optical data. Icarus 149, 329–338. doi:10.100
805 6/icar.2000.6545.

806 Soderblom, J.M., Evans, A.J., Johnson, B.C., Melosh, H.J., Miljković, K.,
807 Phillips, R.J., Andrews-Hanna, J.C., Bierson, C.J., Head, III, J.W., Mil-
808 bury, C., et al., 2015. The fractured Moon: Production and saturation of
809 porosity in the lunar highlands from impact cratering. Geophys. Res. Lett.
810 42, 6939–6944. doi:10.1002/2015GL065022.

Stöffler, D., Ryder, G., Ivanov, B.A., Artemieva, N.A., Cintala, M.J., Grieve, R.A., 2006. Cratering history and lunar chronology. Rev. Mineral. Geochem. 60, 519–596. doi:10.2138/rmg.2006.60.05.

Trowbridge, A.J., Johnson, B.C., Freed, A.M., Melosh, H.J., 2020. Why the lunar South Pole-Aitken basin is not a mascon. Icarus 352, 113995. doi:10.1016/j.icarus.2020.113995.

Tsunakawa, H., Takahashi, F., Shimizu, H., Shibuya, H., Matsushima, M., 2014. Regional mapping of the lunar magnetic anomalies at the surface: Method and its application to strong and weak magnetic anomaly regions. Icarus 228, 35–53. doi:10.1016/j.icarus.2013.09.026.

Wahl, D., Wieczorek, M.A., Wünnemann, K., Oberst, J., 2020. Crustal porosity of lunar impact basins. J. Geophys. Res. Planets 125, e2019JE006335. doi:10.1029/2019JE006335.

Wieczorek, M.A., Neumann, G.A., Nimmo, F., Kiefer, W.S., Taylor, G.J., Melosh, H.J., Phillips, R.J., Solomon, S.C., Andrews-Hanna, J.C., Asmar, S.W., et al., 2013. The crust of the Moon as seen by GRAIL. Science 339, 671–675. doi:10.1126/science.1231530.

Wieczorek, M.A., Phillips, R.J., 1998. Potential anomalies on a sphere: Applications to the thickness of the lunar crust. J. Geophys. Res. Planets 103, 1715–1724. doi:10.1029/97JE03136.

Wieczorek, M.A., Phillips, R.J., 2000. The "Procellarum KREEP Terrane": Implications for mare volcanism and lunar evolution. J. Geophys. Res. Planets 105, 20417–20430. doi:10.1029/1999JE001092.

Wood, C.A., Anderson, L., 1978. New morphometric data for fresh lunar craters. Proc. Lunar Planet. Sci. Conf. 9, 3669–3689.

Xiao, Z., Ding, C., Xie, M., Cai, Y., Cui, J., Zhang, K., Wang, J., 2021. Ejecta from the Orientale basin at the Chang'E-4 landing site. Geophys. Res. Lett. 48, e2020GL090935. doi:10.1029/2020GL090935.

Yue, Z., Shi, K., Di, K., Lin, Y., Gou, S., 2023. Progresses and prospects of impact crater studies. Sci. China Earth Sci. 66, 2441–2451. doi:10.1007/s11430-022-1009-0.

Zhang, M., Fa, W., Eke, V.R., 2023. Modeling the evolution of lunar regolith: 1. Formation mechanism through individual simple impact craters. J. Geophys. Res. Planets 128, e2023JE007850. doi:10.1029/2023JE007850.

Zhang, W., Deng, Q., Ye, M., Hao, W., Chen, Y., et al., 2024. The ancient lithospheric parameters of impact basins on the far side of the Moon based on the mantle and mare basalt load model. J. Geophys. Res. Planets 129, e2023JE008006. doi:10.1029/2023JE008006.

Zuber, M.T., Smith, D.E., Neumann, G.A., Goossens, S., Andrews-Hanna, J.C., Head, J.W., Kiefer, W.S., Asmar, S.W., Konopliv, A.S., Lemoine, F.G., et al., 2016. Gravity field of the Orientale basin from the Gravity Recovery and Interior Laboratory Mission. Science 354, 438–441. doi:10.1126/science.aag0519.

Supplementary Files

This is a list of supplementary files associated with this preprint. Click to download.

- article1enepslsupplementaryinformation.pdf